

Oxygen-rich interface enables reversible stibium stripping/plating chemistry in aqueous alkaline batteries

Haozhe Zhang^{1,3}, Qiyu Liu^{1,3}, Dezhou Zheng², Fan Yang¹, Xiaoqing Liu¹ & Xihong Lu¹✉

Aqueous alkaline batteries see bright future in renewable energy storage and utilization, but their practical application is greatly challenged by the unsatisfactory performance of anode materials. Herein, we demonstrate a latent Sb stripping/plating chemistry by constructing an oxygen-rich interface on carbon substrate, thus providing a decent anode candidate. The functional interface effectively lowers the nucleation overpotential of Sb and strengthens the absorption capability of the charge carriers (SbO_2^- ions). These two advantageous properties inhibit the occurrence of side reactions and thus enable highly reversible Sb stripping/plating. Consequently, the Sb anode delivers theoretical-value-close specific capacity ($627.1 \text{ mA h g}^{-1}$), high depth of discharge (95.0%) and maintains 92.4% coulombic efficiency over 1000 cycles. A robust aqueous NiCo_2O_4 //Sb device with high energy density and prominent durability is also demonstrated. This work provides a train of thoughts for the development of aqueous alkaline batteries based on Sb chemistry.

¹MOE of the Key Laboratory of Bioinorganic and Synthetic Chemistry, The Key Lab of Low-carbon Chem & Energy Conservation of Guangdong Province, School of Chemistry, Sun Yat-Sen University, 510275 Guangzhou, People's Republic of China. ²School of Applied Physics and Materials, Wuyi University, 529020 Jiangmen, People's Republic of China. ³These authors contributed equally: Haozhe Zhang, Qiyu Liu. ✉email: luxh6@mail.sysu.edu.cn

Demanding requirements for renewable energy storage/utilization greatly stimulate the boom of economical, safe, and efficient batteries^{1–5}. With the ever-growing energy consumption, the levelized energy cost (LEC), the economic cost per kW h delivered as output over the entire lifespan of the devices, has become the most important indicator of the batteries^{6–9}. Therefore, to evaluate the overall performance of the energy storage devices, several parameters need to be taken into account together, including the initial capital cost, specific energy, and cycling ability. Along this line, rechargeable aqueous alkaline batteries (AABs), the devices that realize energy storage via the faradaic reactions of electrodes in alkaline electrolyte, emerge as one of the most promising next-generation candidates for renewable energy storage, especially for large-scale applications^{10,11}. This should be ascribed to the advantageous properties of aqueous electrolytes including high ionic conductivity ($\sim 1 \text{ S cm}^{-1}$), low cost, and intrinsic nonflammability¹². Over the past years, tremendous research attention has been paid to the exploration of various electrode materials for AABs, and significant achievements have been gained in this field^{13–16}. Compared with the booming cathode materials, the choice of anode materials remains quite limited and their development is relatively slow.

Currently, based on the disparate differences of their energy storage behavior, the reported anodes are mainly classified into two categories: conversion-type ones and stripping/plating-type ones. Conversion-type anodes such as Cd¹⁷, Bi^{18,19}, and FeO_x^{20,21} experience phase conversion (usually from metal/metal oxide to their corresponding metal oxide/hydroxide) during the charging–discharging process. Yet, the intrinsically poor conductivity and slow reaction kinetics of the metal oxides/hydroxides lead to low capacity and limited rate capability. In contrast, Zn anodes, the most representative stripping/plating-type electrodes, are not bothered by such troubles because they rely on the transformation of metal/metal ions for energy storage, which ensures fast reaction kinetics^{22–24}. Unfortunately, due to the uncontrollable dendrite growth of Zn and the accompanying side reactions, this metal anode suffers from inferior cycling stability and low coulombic efficiency (CE), seriously impeding its further development²⁵. Therefore, it is of great significance to explore novel anode materials embedding both high energy and favorable stability to facilitate the practical applications of AABs in renewable energy storage/utilization, which remains a great challenge in this area.

Stibium (Sb) metal is a desirable anode material owing to its high theoretic capacity (660 mA h g^{-1} , based on three-electron transfer reaction), favorable negative redox potential in alkaline solution (-0.66 V vs. the standard hydrogen electrode) and low cost ($\sim 7\$$ per kg)^{26,27}. Furthermore, according to the ϕ -pH diagram for H₂O–Sb and previous studies, the Sb (III) will exist as soluble SbO₂[−] rather than Sb₂O₃ precipitate in aqueous alkaline environment, which endows Sb metal the capability to function more like the stripping/plating-type anodes with fast kinetics in AABs^{28–31}. To our knowledge, there is hardly any report on the employment of metallic Sb as electrode in aqueous systems, let alone in AABs. For a Sb-based AAB device, there exists strong electrostatic repulsion force between the charge carriers (SbO₂[−]) and the electrode surface, both negatively charged during the plating courses. Such specific interaction makes it difficult for SbO₂[−] ions to approach the anode for proper deposition, and might initiate severe side reactions such as hydrogen evolution. Hence, the key challenge lies in how to manipulate precisely the behaviors of SbO₂[−] ions at the interface.

Herein, by constructing a functional oxygen-rich interface, we realize highly reversible stripping/plating chemistry of Sb metal anode on the carbon substrate (denoted as CS) in AABs. Oxygen-

containing functional groups facilitate the diffusion and deposition behaviors of SbO₂[−] ions on the carbon surface via two ways: (i) to promote the absorption of the SbO₂[−] at the interface by activating the formation of hydrogen bonds; (ii) to decrease the deposition resistance of Sb by minimizing the nucleation overpotential on the anode. Benefiting from these two merits, the potential side reactions are substantially inhibited and highly reversible deposition/dissolution of Sb is realized on the functionalized carbon substrate (denoted as FCS). As a result, the Sb/FCS anode delivers a high specific capacity of $627.1 \text{ mA h g}^{-1}$ ($\sim 95.0\%$ depth of discharge, DOD), along with admirable CE ($\sim 95.9\%$) and satisfactory cycling durability (92.4% CE after 1000 cycles). When coupled with a phosphating NiCo₂O₄ (denoted as P-NiCo₂O₄) cathode, the electrochemical performance of the AAB device outperforms most recently reported AABs, as testified by its superior energy density (8.2 mW h cm^{-3}), excellent power density (0.4 W cm^{-3}), as well as its admirable stability (98.1% capacity retention over 1000 cycles). This work opens a favorable way for the exploration of novel Sb-based aqueous devices as power supply systems.

Results

Stripping/plating chemistry studies of stibium. The stripping/plating chemistry of Sb on different substrates is compared in Fig. 1a. Because the Sb (III) will exist as SbO₂[−] without forming tartrate–Sb complex in potassium antimony tartrate–KOH aqueous system, the simplified schematic illustration only shows the K⁺ and SbO₂[−] for demonstration²⁸. For the CS substrate, at the very beginning, the disordered molecular thermodynamic motion of the SbO₂[−] ions leads to their random distribution in the electrolyte. Upon charging the anode, the SbO₂[−] ions in the Helmholtz layer are reduced to Sb on the substrate, and the as-deposited Sb metal would resolve into the electrolyte during the discharging course. It is noteworthy that, in the charging process, a large portion of SbO₂[−] ions would migrate toward the counter electrode instead of the deposition substrate, leading to catastrophic plating efficiency or even side reactions. This should be attributed to the strong electrostatic repulsion between the charge carriers (SbO₂[−]) and the negatively-charged CS surface. Therefore, to enable highly reversible stripping/plating chemistry of Sb, it is essential to design a functionalized carbon interface that is capable of “capturing” tightly the SbO₂[−] in the close vicinity of the electrode at the deposition stage. To achieve this goal, we decorate the CS with some oxygen-containing functional groups via a facile electrochemical activation strategy. As shown in Supplementary Fig. 1, the untreated CS consisting of interlaced carbon fibers exhibits a smooth surface and it becomes relatively rough after electrochemical treatment. The Brunauer–Emmett–Teller surface areas of both samples shown in Supplementary Fig. 2 remain small values, but which of FCS becomes slightly larger after the treatment (from 1.4 to $3.2 \text{ m}^2 \text{ g}^{-1}$). The introduction of oxygen functional groups in FCS is accompanied by the generation of graphene edges with thickness of about 10 nm (Supplementary Fig. 3). In addition, the X-ray diffraction (XRD) spectra of CS and FCS (Supplementary Fig. 4) are both perfectly indexed to hexagonal graphite (JCPDF#41-1487), indicating their similar crystalline structure³². Yet, the detailed X-ray photoelectron spectroscopy (XPS) analysis of the C 1s peak reveals that the electrochemical activation process successfully introduces oxygen atoms to the FCS surface in the form of C–OH (285.7 eV), C=O (286.9 eV), and O–C=O (288.7 eV) (Supplementary Fig. 5)³³. Congruously, the intensity of O 1s peak for the FCS (O/C ratio = 0.17) is also much higher than the CS (O/C ratio = 0.04). Electrochemical impedance spectra (EIS) in Supplementary Fig. 6 indicates that the charge transfer resistance of FCS is slightly increased, consistent with the previous work³². Nevertheless, the

oxygen-rich interface holds great potential for boosting the Sb deposition because it can provide abundant receptors and donors for the formation of hydrogen bonds that favors the adsorption of SbO_2^- ions in the Helmholtz layer.

The working potential window of the CS and FCS electrodes in 1 M KOH with 0.027 M $\text{C}_8\text{H}_4\text{K}_2\text{O}_{12}\text{Sb}_2$ was tested by linear sweep voltammetry (LSV) at 1 mV s^{-1} . As shown in Supplementary Fig. 7, the H_2 evolution reactions on both two electrodes take place at around -1.5 V , so the potential window of 0 to -1.3 V was selected to avoid water splitting. Cyclic voltammograms (CV) within this voltage window were recorded on the CS and FCS at 2 and 10 mV s^{-1} to study the stripping/plating chemistry of Sb (Supplementary Fig. 8). Both electrodes possess one redox couple whereas smaller voltage polarization is visualized on the FCS sample, indicating its higher reversibility. Further chemical composition investigation verifies the redox couple corresponds to the deposition/dissolution of Sb (Fig. 1b–g and Supplementary Fig. 9). Specifically, when the charging capacity is set to $0.47 \text{ mA h cm}^{-2}$, the precipitates on both electrodes are confirmed to be pure hexagonal $R\text{-}3\text{m}$ phase Sb without other impurities (JCPDS#85-1322, Supplementary Fig. 10)^{34,35}. The high-resolution transmission electron microscopy (HRTEM) characterization in Supplementary Fig. 11 further testifies this viewpoint. The lattice spacing of 0.31 nm matches well with the (012) plane of hexagonal Sb (JCPDS#85-1322), while the bright diffraction and highly-ordered spots in the selected-area electron diffraction (SAED) patterns indicate its good crystallinity³⁶. When the electrodes are discharged to 0 V (discharging state), Sb metal are nearly completely dissolved back to the electrolyte. Notably, in the charging stage, the Sb metal (Fig. 1d) deposits as randomly-distributed, isolated nanoflowers, leaving some uncovered spaces on the CS. In contrast, the deposition of Sb seems more homogeneous on the entire surface of the FCS (Fig. 1e), indicative of the superiority of the oxygen-decorated functional interface. The Sb/ SbO_2^- transformation during the charging/discharging is also verified by the *ex situ*

XRD spectra (Supplementary Fig. 12), in which the characteristic peaks of metallic Sb disappear at the discharging state and recover at the charging state.

To highlight the superiority of the FCS over the CS, their electrochemical behaviors are compared with a fixed charging capacity of $0.47 \text{ mA h cm}^{-2}$. At a current density of 30 mA cm^{-2} , the charge limited voltage (V_{cl}) of Sb/CS, which means the voltage attained at the end of charging (absolute value), reaches a high value of 1.50 V within merely 50 cycles and increases to 1.70 V after 500 cycles, accompanied by severe hydrogen evolution (Supplementary Fig. 13). The Sb/FCS electrode shows a stable charging voltage profile, along with a low V_{cl} about 1.25 V for 1000 cycles (Fig. 2a). At a smaller current density of 20 mA cm^{-2} (Fig. 2b), the hydrogen evolution of the Sb/CS electrode is intensified, resulting in a high V_{cl} of 1.55 V after only ten cycles. In contrast, the V_{cl} of the Sb/FCS electrode is only 1.30 V after 1000 cycles (Supplementary Fig. 14), signifying its better cycling durability. Moreover, it should be noticed that the test duration of Sb/FCS at both current densities lasts much longer than Sb/CS. The charging time and cycling numbers of Sb/CS and Sb/FCS are the same, so the longer test time means longer average discharging time, manifesting longer average discharging time and better CE of Sb/FCS.

According to the discharging curves at 20 mA cm^{-2} in Fig. 2c, the Sb/CS show a capacity of $\sim 0.32 \text{ mA h cm}^{-2}$ at the first 50 cycles. When the cycling test is extended from 100 to 1000 cycles, it fades rapidly from 0.18 to $0.05 \text{ mA h cm}^{-2}$, signifying the irreversible plating/stripping courses. Obviously, the Sb/FCS maintains a much larger discharging capacity in the range of $0.42\text{--}0.45 \text{ mA h cm}^{-2}$ during the 1000 cycles. At lower current density conditions ($2\text{--}8 \text{ mA cm}^{-2}$), the discharging capacities of Sb/FCS can even achieve more than $0.46 \text{ mA h cm}^{-2}$ (Supplementary Fig. 15). It is worth noting that the capacitive charge contribution of both CS and FCS only account for ignorable percentage comparing with the discharging capacity of Sb/CS ($\sim 1.3\%$) and Sb/FCS ($\sim 2.8\%$), indicating the capacities are mainly

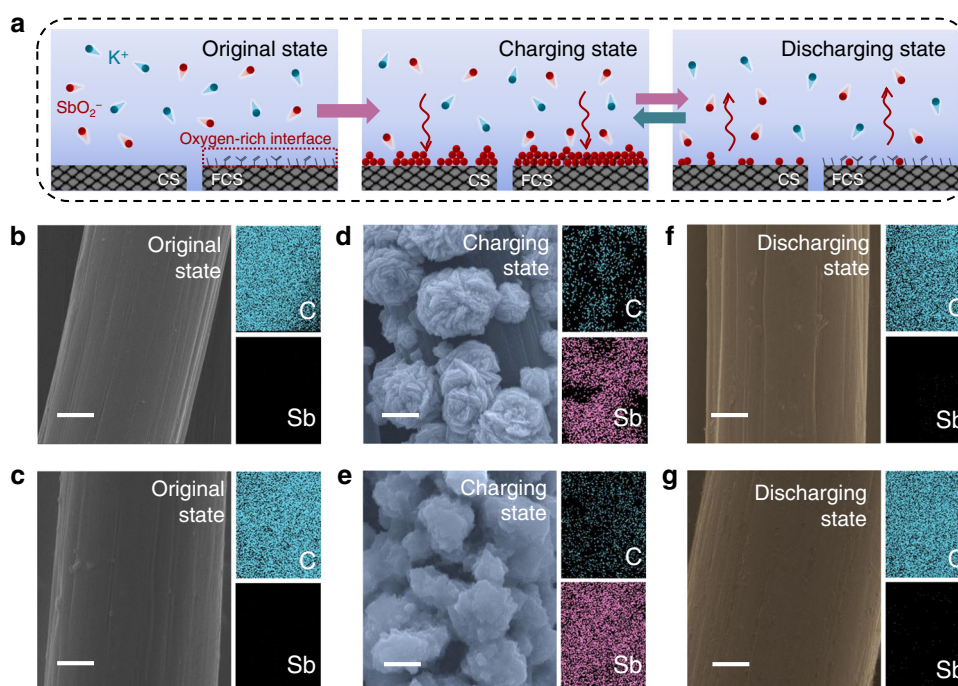


Fig. 1 Charge storage mechanism investigations of stibium. **a** Schematic illustration of the charge storage mechanism of the Sb anode in 1 M KOH and 0.027 M $\text{C}_8\text{H}_4\text{K}_2\text{O}_{12}\text{Sb}_2$ electrolyte. The arrows indicate the direction of Sb metal stripping/plating. **b–g** SEM images and mapping of **b** CS and **c** FCS in original state; **d** Sb/CS and **e** Sb/FCS in charging state; **f** Sb/CS and **g** Sb/FCS in discharging state. Scale bars: $2 \mu\text{m}$.

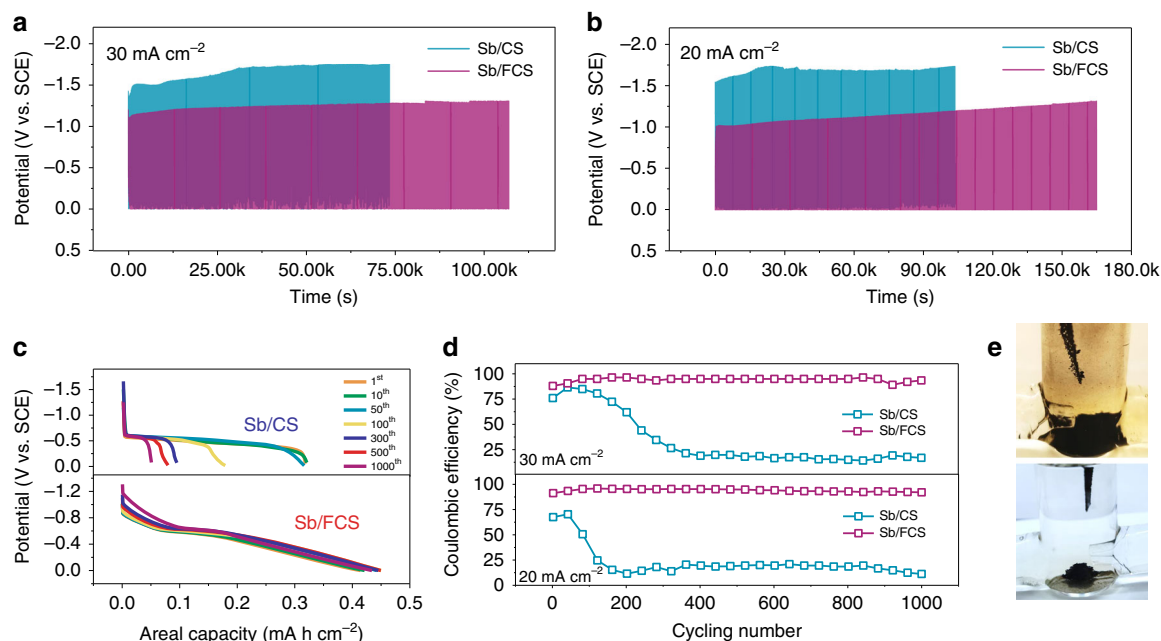


Fig. 2 Electrochemical characterizations of Sb/CS and Sb/FCS electrodes. Voltage profiles of Sb/CS and Sb/FCS with a fixed charging capacity of $0.47 \text{ mA h cm}^{-2}$ at **a** 30 mA cm^{-2} (55 s charging) and **b** 20 mA cm^{-2} (85 s charging). **c** Corresponding discharging curves at different cycles at 20 mA cm^{-2} and **d** CE of the Sb stripping/plating on the bare CS and FCS. **e** Optical photographs of Sb/CS and Sb/FCS after 1000 cycles at 20 mA cm^{-2} .

come from the stripping/plating process of Sb (Supplementary Fig. 16). Additionally, an impressive DOD of 95% and a superb specific capacity of $627.1 \text{ mA h g}^{-1}$ are achieved by the Sb/FCS anode (based on the mass loading of Sb), outstripping various anodes of aqueous batteries. Besides, the CE (the ratio of Sb stripping capacity to Sb plating capacity) of the two samples are also presented in Fig. 2d to elucidate the sustainability of the electrodes. As expected, at 20 or 30 mA cm^{-2} , the CE of FCS electrode remains to be 92–95% without attenuation after 1000 cycles. In comparison, the CE of the CS electrode drops to less than 20% very shortly at both current densities. Such disappointed performance might be caused by the occurrence of severe side reactions. The morphology characterization of the electrodes after cycling tests shows that the deposition/dissolution processes of Sb on the CS are irreversible, leaving much more black sediments (insoluble “dead Sb”) (Fig. 2e)³⁷. Yet, no obvious difference is seen on the FCS before and after the stability test (Supplementary Fig. 17). It is thus comprehensively demonstrated that the oxygen-rich interface of FCS could restrict the side reactions and guide the reversible stripping/plating chemistry of Sb.

Insights into reversible stripping/plating process. The role of the oxygen-rich interface of FCS in inducing reversible Sb stripping/plating chemistry was then investigated theoretically by density functional theory (DFT) calculations. During the plating process, the absorption properties of SbO_2^- on the substrate surface have a vital effect on the Sb/ SbO_2^- conversion reaction. Figure 3a describes the absorption energy of the SbO_2^- for the CS surface with or without the introduction of the oxygen-containing functional groups. Remarkably, the surfaces with all kinds of functional groups including $>\text{C}=\text{O}$ (-2.0 eV), $>\text{C}-\text{OH}$ (-1.6 eV) and $-\text{COOH}$ (-2.1 eV) possess much lower absorption energy than that of the bare CS (-0.9 eV). Therefore, the FCS surface is very likely to gather more SbO_2^- ions in the Helmholtz layer, which would significantly enhance the Sb plating efficiency. As a proof of concept, when fixing the charging capacity at $0.47 \text{ mA h cm}^{-2}$, the electrochemical reactions on CS can be divided into

two stages (Fig. 3b): (i) at around -1.0 V , an efficient Sb deposition accounts for $0.17 \text{ mA h cm}^{-2}$; (ii) with the rapid potential increase to -1.6 V , the hydrogen evolution side reaction (HER) makes up the rest capacity of $0.30 \text{ mA h cm}^{-2}$. This point can be further proved by the weight variation of CS electrode during the charging process (Supplementary Fig. 18). As illustrated in Fig. 3c, d, when the CS is negatively charged for Sb plating, the strong electrostatic repulsion force repels the SbO_2^- ions to diffuse away from the anode surface. When the few SbO_2^- ions left in the Helmholtz layer is completely consumed by initial Sb deposition, water decomposition reaction will be launched alternatively due to the lack of Sb source, leading to serious hydrogen evolution and active material shedding. Benefitting from the oxygen-rich functional interface, the supplementary of SbO_2^- in the Helmholtz layer would be substantially more effective on the FCS during the plating. Under this circumstance, the FCS enables an efficient Sb deposition up to $0.47 \text{ mA h cm}^{-2}$ at a low cut-off charge voltage of -1.0 V (Fig. 3b), getting rid of the interference of HER and thus achieving a high CE. This is highly consistent with the XPS C 1s spectra at the charging state in Supplementary Fig. 19, in which the Sb/FCS holds a raised quantity of C–Sb bonds (C–Sb: C–C = $0.61\text{--}0.27$) compares with the Sb/CS³⁸. Moreover, the deposition of Sb on FCS can be divided into two stages: (i) 0 to -0.95 V and (ii) -0.95 to -1.0 V . As revealed by the weight variation curve and *ex situ* scanning electron microscopy (SEM) images of the charging process in Supplementary Fig. 20, the electrochemical deposition of Sb take place on FCS at both stages. The first stage (0 to -0.95 V) might be attributed in an underpotential deposition (UPD)-like process, while the other stage (-0.95 to -1.0 V) is normal deposition process. The nucleation stage is a pivotal step for fully understanding the deposition behaviors of Sb on different substrates³⁹. We then compare the nucleation overpotential disparities of CS and FCS to illuminate the role of oxygen-rich functional interface in modulating Sb nucleation. The nucleation overpotential is defined as the voltage difference between the lowest voltage, when sharp voltage drops take place and equilibrium potential in the galvanostatic cathodic polarization. As shown in Supplementary

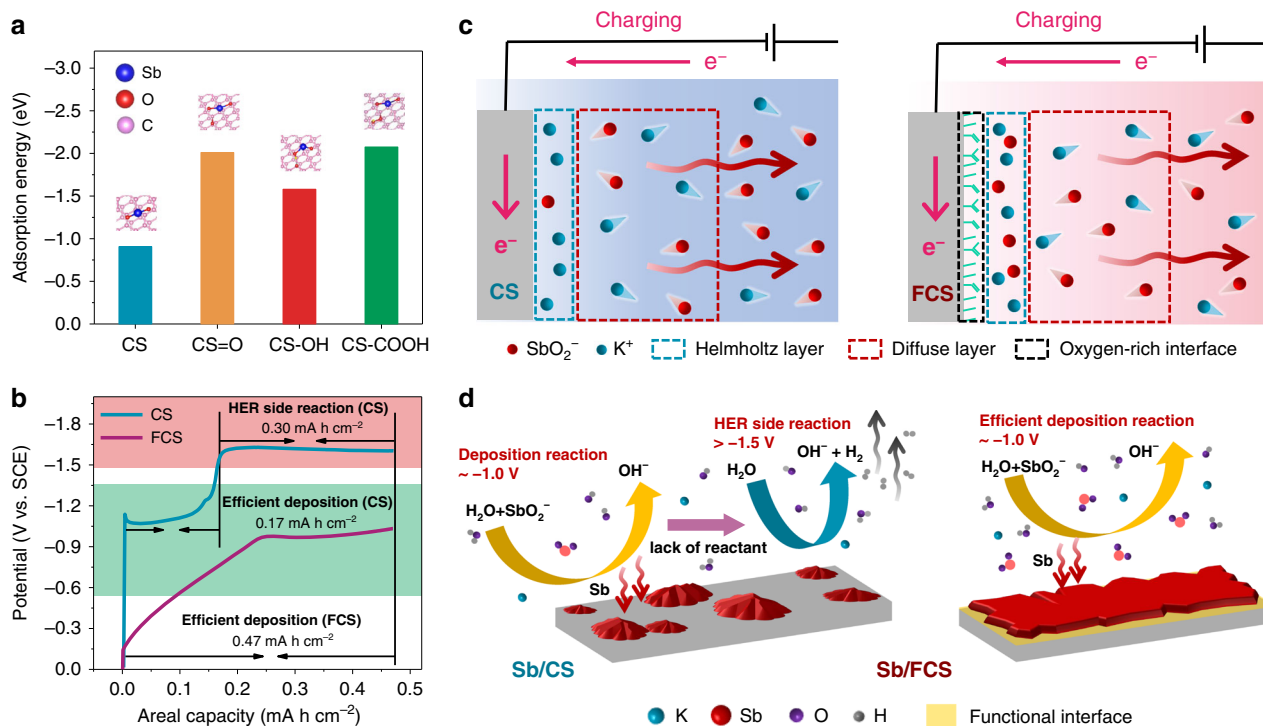


Fig. 3 Comprehension of oxygen-rich interface induced reversible stripping/plating process. **a** Relative SbO₂⁻ absorption energy profiles of the CS surface with different functional groups. **b** Electroplating curve of the Sb on the substrates at 20 mA cm⁻² with a fixed charging capacity of 0.47 mA h cm⁻². **c** Illustration of the ion distribution during the plating process of CS and FCS. The arrows indicate the direction of SbO₂⁻ diffusion. **d** The plating mechanism on the substrate with/without the functional interface induced.

Fig. 21, with respect to the CS, the profile of FCS delivers a smoother voltage dip and a much lower nucleation overpotential (from 147 to 29 mV), suggesting the oxygen-rich functional interface can dramatically lower the resistance for Sb nucleation and is more favorable for Sb deposition. Briefly, the FCS integrates the strong absorption capability of the SbO₂⁻ and the lower Sb nucleation overpotential, which conjointly contribute to the suppression of side reactions and the high efficiency of Sb stripping/plating.

Process performance of NiCo//Sb aqueous alkaline battery. In order to further demonstrate the potential of Sb/FCS electrode in energy storage applications, we assembled an AAB device (denote as NiCo//Sb battery) by employing Sb/FCS as anode and P-NiCo₂O₄ (see details in Supplementary Fig. 22 and see “Methods” section) as cathode⁴⁰. Figure 4a shows the CV curves of the cathode and the anode at 10 mV s⁻¹. The large potential difference between the two electrodes brings about a high discharging platform of ~1.0 V, which is consistent with the CV results of NiCo//Sb battery (Supplementary Fig. 23). The energy storage mechanism of the NiCo//Sb battery is illustrated in Fig. 4b, in which the cathode proceeds redox reactions while the anode undergoes stripping/plating process (Supplementary Note 1)^{22,31,41}.

It is noteworthy that the as-fabricated battery delivers a large areal capacity of 0.75 mA h cm⁻² at 8 mA cm⁻² (Fig. 4c). With the increase of the current density to an ultrahigh level of 36 mA cm⁻², 0.21 mA h cm⁻² capacity is still retained with only 21 s discharging, reflecting its good rate ability. When the active material mass of both electrodes is counted, the NiCo//Sb AAB also reaches a high specific capacity of 175.6 mA h g⁻¹, superior to recently reported AABs shown in Fig. 4d^{19–21,42,43}. Furthermore, a maximum volumetric energy density of 8.2 mW h cm⁻³ and a maximum volumetric power density of 0.4 W cm⁻³ have been achieved of the

battery (based on combined volume of cathode and anode), which considerably surpass a series of AABs (Fig. 4e), like Ni–NiO//BiO_x battery (1.6 mW h cm⁻³, 0.44 W cm⁻³)¹⁸, NiCo₂O₄//Bi battery (1.5 mW h cm⁻³, 0.02 W cm⁻³)¹⁹, NCHO (nickel cobalt hydroxide)//Zn battery (2.2 mW h cm⁻³, 0.05 W cm⁻³)⁴⁴, Ni(OH)₂//FeO_x battery (2.5 mW h cm⁻³, 0.03 W cm⁻³)²⁰, Ni/N-doped C//Zn battery (0.66 mW h cm⁻³, 0.13 W cm⁻³)⁴⁵, NiO//Fe₃O₄ battery (5.2 mW h cm⁻³, 0.08 W cm⁻³)²¹, Ni/Ni(OH)₂//Zn battery (2.9 mW h cm⁻³, 0.14 W cm⁻³)⁴⁶. More encouragingly, our NiCo//Sb battery also exhibits outstanding long-term cycling stability with a slight capacity fading (~1.9%) after 1000 cycles (Fig. 4f), as well as a high CE (95.7%). The charge/discharge profiles of the battery at the initial, middle and final stages remain almost the same in the voltage plateaus and charging/discharging times, again demonstrating its remarkable reversibility and stability.

Discussion

In summary, we demonstrated a highly reversible stripping/plating chemistry of Sb and thus provide a promising electrolytic metallic Sb anode for AABs. The diffusion behaviors of SbO₂⁻ ions at the interface are effectively manipulated by an oxygen-rich functional interface, which could not only significantly promote the surface absorption of SbO₂⁻ in the Helmholtz layer to restrain the side reaction and increase the CE; but also, lower the nucleation overpotential and induce the uniform Sb deposition. As a consequence, the Sb/FCS anode delivered an obviously improved durability with an excellent CE of more than 92.4% during the 1000 cycles, associated with a remarkable specific capacity of 627.1 mA h g⁻¹ at 0.47 mA h cm⁻² (~95.0% DOD). Moreover, the as-prepared NiCo//Sb AAB device delivered a prominent stability (98.1% capacity retention after 1000 cycles), an outstanding maximum volumetric energy density (8.2 mW h cm⁻³) along with a peak power density (0.4 W cm⁻³), surpassing many of the state-of-the-art AABs reported recently. The development of the

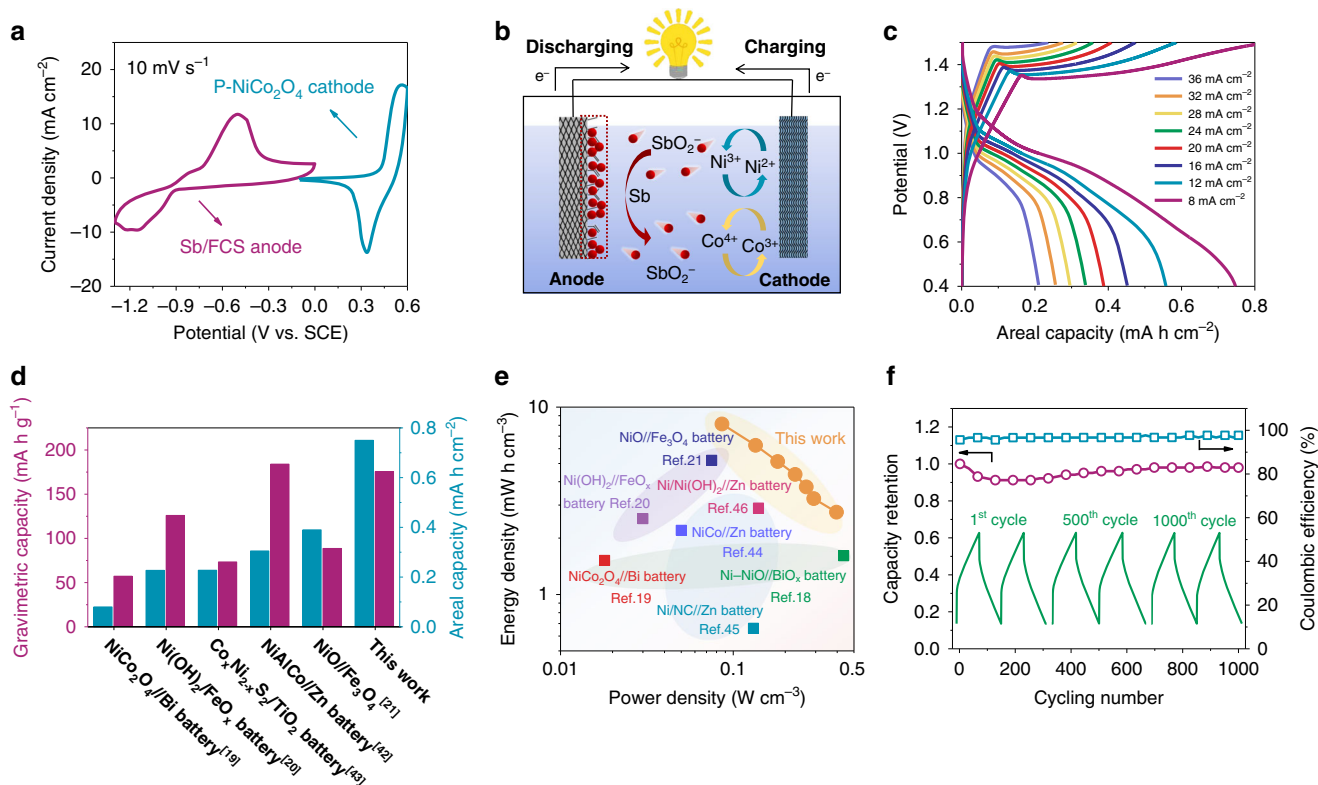


Fig. 4 Electrochemical performance of assembled AAB using Sb/FCS anode. **a** CV curves of the P-NiCo₂O₄ cathode and Sb/FCS anode measured at 10 mV s⁻¹. **b** The energy storage mechanism of the NiCo//Sb battery. **c** Galvanostatic charge-discharge (GCD) curves at different current densities, **d** areal capacity and gravimetric capacity comparison with previous studies^{19–21,42,43}, **e** Ragone plots, the values reported for other energy storage devices are added for comparison^{18–21,44–46} and **f** the cycling stability of the NiCo//Sb battery.

promising Sb anode in our work will be of immediate benefit to the exploration of high-performance AABs for practical utilization, particularly, for grid-scale energy storage.

Methods

Preparation of electrolyte. All reagents are of analytical grade and are directly used without any purification. 0.5 g of potassium antimony tartrate (C₈H₄K₂O₁₂Sb₂) is dissolved in 30 ml 1 M KOH, resulting in a mixture of 1 M KOH and 0.027 M C₈H₄K₂O₁₂Sb₂. The reaction equation for the formation of SbO₂⁻ is listed in Supplementary Note 2.

Preparation of CS and FCS electrodes. The CS substrate is purchased directly from Fuel Cell Earth, USA (plain carbon fiber cloth; 12.6 mg cm⁻²). Subsequently, the FCS substrate is obtained by CS after an electrochemical functional group introducing process. First, the CS is ultrasonic in water and ethanol for 10 min and undergoing controllable Ar plasma process by atomic layer deposition (ALD) technology (ALD-SC6-PE, Syskey Technology Co., Ltd.) to produce clean surface. The electrochemical functional group introducing is then carried out through a standard three-electrode system in a solution composed by H₂SO₄ (98%) and HNO₃ (68%) with a volume ratio of 1:1. The system uses Pt electrode as the counter electrode, saturated calomel electrode (SCE) as the reference electrode and CS as the working electrode. The electrochemical functional group introducing process is conducted with a constant voltage of 3 V for 15 min at the room temperature. The FCS is washed with deionized water after the process and dried in the oven at 60 °C for 3 h.

Preparation of P-NiCo₂O₄ cathode. P-NiCo₂O₄ is obtained by a previously reported hydrothermal and annealing method growing on nickel foam. Initially, urea (15 mmol), NiCl₂·6H₂O (5 mmol), and CoCl₂·6H₂O (10 mmol) are dissolved in 75 ml deionized water under vigorous magnetic stirring. After the mixture is clarified, 35 ml solution is added into a 50 ml Teflon-lined stainless steel autoclave with a piece of cleaned nickel foam (2.7 cm × 4 cm). The autoclave is heated at 120 °C for 6 h and then cooled down to room temperature. After washed with deionized water and dried at 70 °C in air, the prepared NiCo₂O₄ is calcined at 300 °C for 2 h and the heating rate was 2 °C min⁻¹. To get P-NiCo₂O₄, the obtained samples are annealed at 250 °C for

60 min in Ar atmosphere in the presence of NaH₂PO₄·H₂O (1.2 g). The mass loading of the P-NiCo₂O₄ is 3.1 mg cm⁻² (BT25S, 0.01 mg), and the thickness of the cathode after tableting is 0.04 cm.

Electrochemical measurements. Galvanostatic charge/discharge curves (GCD) and cyclic voltammogram (CV) are recorded using Neware battery system (CT-3008-5V10mA-164, Shenzhen, China) and electrochemical work-station (CHI 760E). The Princeton electrochemical workstation (PARSTAT MC) was used to collect Electrochemical impedance spectroscopy (EIS). All electrochemical characterization is performed at room temperature. For Sb plating/stripping test, CS and FCS substrates are used as working electrode with a surface area of 0.5 cm², graphite rod was employed as counter electrode, and SCE as the reference electrode in three-electrode system. The electrolyte is a mixed solution of 1 M KOH and 0.027 M C₈H₄K₂O₁₂Sb₂. The charging process is achieved by a galvanostatic charging method to charge a fixed value (0.47 mA h cm⁻²) and the discharging process is achieved by a galvanostatic discharging method to discharge to 0 V. The mass loadings of Sb/CS and Sb/FCS deposition electrodes are 0.64 mg cm⁻² and 0.71 mg cm⁻², respectively while charging 0.47 mA h cm⁻² (BT25S, 0.01 mg). The aqueous NiCo//Sb battery is tested in two-electrode system with the same electrolyte, using P-NiCo₂O₄ as cathode and FCS substrate as anode. The mass loading of Sb/FCS electrode at 8 mA cm⁻² is 1.1 mg cm⁻². Calculations about capacity, energy density and power density of Sb anode and NiCo//Sb battery are shown in Supplementary Note 3.

Material characterization. Field-emission SEM (SEM, JSM-6330F and SEM, g-500) and TEM (FEI Tecnai G² F30) are used to character the morphology and the microstructure of the deposited Sb on the substrate. XRD (D-MAX 2200 VPC, RIGAKU), XPS (NEXSA, Thermo FS) are used to character the crystal phase and composition of the deposited Sb on the substrate.

Computational details. All the calculations were performed using the Vienna Ab-initio Simulation Package (VASP). The generalized gradient approximation (GGA) in the scheme of Perdew–Burke–Ernzerhof (PBE) function was used to calculate the electron exchange–correlation interactions. The cutoff energy for plane-wave basis set was set to 400 eV. All atomic positions and lattice vectors were fully optimized using a conjugate gradient algorithm to obtain the unstrained

configuration. Atomic relaxation was performed until the change of total energy was less than 1×10^{-5} eV, all the forces on each atom were smaller than 0.01 eV/Å. The adsorbed surface was used (002) slab with 12 Å vacuum in the c-direction to eliminate periodic boundary interaction. Monkhorst–Pack scheme K-point grid was set to $3 \times 3 \times 1$ during surface relaxation.

Data availability

The data that support the findings of this study are available from the corresponding authors upon reasonable request.

Received: 3 July 2020; Accepted: 11 November 2020;

Published online: 04 January 2021

References

- Li, Y. et al. Growth of conformal graphene cages on micrometre-sized silicon particles as stable battery anodes. *Nat. Energy* **1**, 1–8 (2016).
- Li, Z. et al. A sulfur host based on titanium monoxide@carbon hollow spheres for advanced lithium–sulfur batteries. *Nat. Commun.* **7**, 13065 (2016).
- Wan, F. & Niu, Z. Design strategies for vanadium-based aqueous zinc-ion batteries. *Angew. Chem. Int. Ed.* **58**, 16358–16367 (2019).
- Suo, L. et al. “Water-in-salt” electrolyte enables high-voltage aqueous lithium-ion chemistries. *Science* **350**, 938–943 (2015).
- Zhang, H. et al. Boosting Zn-ion energy storage capability of hierarchically porous carbon by promoting chemical adsorption. *Adv. Mater.* **31**, 1904948 (2019).
- Chao, D. et al. An electrolytic Zn-MnO₂ battery for high-voltage and scalable energy storage. *Angew. Chem. Int. Ed.* **58**, 7823–7828 (2019).
- Zhong, C. et al. Decoupling electrolytes towards stable and high-energy rechargeable aqueous zinc–manganese dioxide batteries. *Nat. Energy* **5**, 440–449 (2020).
- Hong, J. J. et al. A dual plating battery with the Iodine/[ZnI_x(OH)₂]_{4-x} cathode. *Angew. Chem. Int. Ed.* **131**, 2–8 (2019).
- Zhang, Y. et al. Multiscale graphene-based materials for applications in sodium ion batteries. *Adv. Energy Mater.* **9**, 1803342 (2019).
- Zeng, Y. et al. An ultrastable and high-performance flexible fiber-shaped Ni-Zn battery based on a Ni-NiO heterostructured nanosheet cathode. *Adv. Mater.* **29**, 1702698 (2017).
- Parker, J. F. et al. Rechargeable nickel–3D zinc batteries: an energy-dense, safer alternative to lithium-ion. *Science* **356**, 415–418 (2017).
- Zhang, X. et al. Oxygen defect modulated titanium niobium oxide on graphene arrays: an open-door for high-performance 1.4 V symmetric supercapacitor in acidic aqueous electrolyte. *Adv. Funct. Mater.* **28**, 1805618 (2018).
- Wang, M. et al. Making fiber-shaped Ni//Bi battery simultaneously with high energy density, power density, and safety. *Adv. Funct. Mater.* **30**, 1905971 (2019).
- Liu, J. et al. A flexible quasi-solid-state nickel-zinc battery with high energy and power densities based on 3D electrode design. *Adv. Mater.* **28**, 8732–8739 (2016).
- Li, M. et al. Finely crafted 3D electrodes for dendrite-free and high-performance flexible fiber-shaped Zn-Co batteries. *Adv. Funct. Mater.* **28**, 1802016 (2018).
- Ma, L. et al. Initiating a mild aqueous electrolyte Co₃O₄/Zn battery with 2.2 V-high voltage and 5000-cycle lifespan by a Co(III) rich-electrode. *Energy Environ. Sci.* **11**, 2521–2530 (2018).
- García-Plaza, M., Serrano-Jiménez, D., Eloy-García Carrasco, J. & Alonso-Martínez, J. A Ni–Cd battery model considering state of charge and hysteresis effects. *J. Power Sources* **275**, 595–604 (2015).
- Zeng, Y. et al. Engineering high reversibility and fast kinetics of Bi nanoflakes by surface modulation for ultrastable nickel-bismuth batteries. *Chem. Sci.* **10**, 3602–3607 (2019).
- Zeng, Y. et al. Flexible ultrafast aqueous rechargeable Ni//Bi battery based on highly durable single-crystalline bismuth nanostructured anode. *Adv. Mater.* **28**, 9188–9195 (2016).
- Wang, H. et al. An ultrafast nickel-iron battery from strongly coupled inorganic nanoparticle/nanocarbon hybrid materials. *Nat. Commun.* **3**, 917 (2012).
- Guan, C. et al. High-performance flexible solid-state Ni/Fe battery consisting of metal oxides coated carbon cloth/carbon nanofiber electrodes. *Adv. Energy Mater.* **6**, 1601034 (2016).
- Zeng, Y. et al. Oxygen-vacancy and surface modulation of ultrathin nickel cobaltite nanosheets as a high-energy cathode for advanced Zn-ion batteries. *Adv. Mater.* **30**, 1802396 (2018).
- Yan, Z., Wang, E., Jiang, L. & Sun, G. Superior cycling stability and high rate capability of three-dimensional Zn/Cu foam electrodes for zinc-based alkaline batteries. *RSC Adv.* **5**, 83781–83787 (2015).
- Huang, J. et al. Polyaniline-intercalated manganese dioxide nanolayers as a high-performance cathode material for an aqueous zinc-ion battery. *Nat. Commun.* **9**, 2906 (2018).
- Zeng, Y. et al. In situ activation of 3D porous Bi/carbon architectures: toward high-energy and stable nickel-bismuth batteries. *Adv. Mater.* **30**, 1707290 (2018).
- Li, X., Sun, M., Ni, J. & Li, L. Template-free construction of self-supported Sb prisms with stable sodium storage. *Adv. Energy Mater.* **9**, 1901096 (2019).
- Han, Y. et al. Stabilizing antimony nanocrystals within ultrathin carbon nanosheets for high-performance K-ion storage. *Energy Storage Mater.* **20**, 46–54 (2019).
- Ulrich, N. Speciation of antimony(III), antimony(V) and trimethylstiboxide by ion chromatography with inductively coupled plasma atomic emission spectrometric and mass spectrometric detection. *Anal. Chim. Acta* **359**, 245–253 (1998).
- Wikstrom, L. L. & Nobe, K. Electrode kinetics of antimony in alkaline solutions. *J. Appl. Electrochem.* **14**, 257–263 (1984).
- Vink, B. W. Stability relations of antimony and arsenic compounds in the light of revised and extended Eh-pH diagrams. *Chem. Geol.* **130**, 21–30 (1996).
- Wang, Q. & Wang, Y. Fundamental electrochemical behavior of antimony in alkaline solution. *J. Sustain. Metall.* **5**, 606–616 (2019).
- Wang, W. et al. A novel exfoliation strategy to significantly boost the energy storage capability of commercial carbon cloth. *Adv. Mater.* **27**, 3572–3578 (2015).
- Wang, G. et al. Solid-state supercapacitor based on activated carbon cloths exhibits excellent rate capability. *Adv. Mater.* **26**, 2676–2682 (2014).
- Zhang, N. et al. Spherical nano-Sb@C composite as a high-rate and ultra-stable anode material for sodium-ion batteries. *Nano Res.* **8**, 3384–3393 (2015).
- Luo, W. et al. Bottom-up confined synthesis of nanorod-in-nanotube structured Sb@N-C for durable lithium and sodium storage. *Adv. Energy Mater.* **8**, 1703237 (2018).
- Zhu, J. et al. Controlled synthesis of Sb nanostructures and their conversion to CoSb₃ nanoparticle chains for Li-ion battery electrodes. *Chem. Mater.* **22**, 5333–5339 (2010).
- Zeng, Y. et al. Dendrite-free zinc deposition induced by multifunctional CNT frameworks for stable flexible Zn-ion batteries. *Adv. Mater.* **31**, 1903675 (2019).
- Fei, J. et al. A flexible Sb₂O₃/carbon cloth composite as a free-standing high performance anode for sodium ion batteries. *Chem. Commun.* **53**, 13165–13167 (2017).
- Xie, X. et al. Manipulating the ion-transfer kinetics and interface stability for high-performance zinc metal anodes. *Energy Environ. Sci.* **13**, 503–510 (2020).
- Qiu, W., Xiao, H., Yu, M., Li, Y. & Lu, X. Surface modulation of NiCo₂O₄ nanowire arrays with significantly enhanced reactivity for ultrahigh-energy supercapacitors. *Chem. Eng. J.* **352**, 996–1003 (2018).
- Pješčić, M. G., Šušić, M. V. & Minić, D. Reduction of Sb(III) on the mercury electrode. *Electroanal. Chem. Interfacial Chem.* **57**, 429–432 (1974).
- Gong, M. et al. Ultrafast high-capacity NiZn battery with NiAlCo-layered double hydroxide. *Energy Environ. Sci.* **7**, 2025 (2014).
- Liu, J. et al. Aqueous rechargeable alkaline Co_xNi_{2-x}S₂/TiO₂ battery. *ACS Nano* **10**, 1007–1016 (2016).
- Huang, Y. et al. Weavable, conductive yarn-based NiCo//Zn textile battery with high energy density and rate capability. *ACS Nano* **11**, 8953–8961 (2017).
- Meng, L. et al. Electrochemically activated nickel–carbon composite as ultrastable cathodes for rechargeable nickel–zinc batteries. *ACS Appl. Mater. Interfaces* **11**, 14854–14861 (2019).
- Cheng, X. et al. Facile activation of commercial Ni foil as robust cathode for advanced rechargeable Ni-Zn battery. *Electrochim. Acta* **263**, 311–317 (2018).

Acknowledgements

We thank the financial support by the National Natural Science Foundation of China (21822509, U1810110, and 21802173), Science and Technology Planning Project of Guangdong Province (2018A050506028), and Natural Science Foundation of Guangdong Province (2018A030310301). The calculation of this work was performed on TianHe-2, thanks for the support of National Supercomputing Center in Guangzhou (NSCC-GZ). The authors also thank the Photoemission Endstations (BL10B) in National Synchrotron Radiation Laboratory (NSRL) for help in characterizations.

Author contributions

X.Lu and H.Z. planned and designed the project. H.Z. and Q.L. fabricated the materials and performed the electrochemical experiments. D.Z. performed and analyzed the XPS result.

F.Y. conducted the DFT analysis. X.Lu, H.Z., Q.L., and X.Liu analyzed the data and wrote the manuscript. All authors discussed the results and commented on the manuscript.

Competing interests

The authors declare no competing interests.

Additional information

Supplementary information is available for this paper at <https://doi.org/10.1038/s41467-020-20170-8>.

Correspondence and requests for materials should be addressed to X.L.

Peer review information *Nature Communications* thanks the anonymous reviewer(s) for their contribution to the peer review of this work. Peer reviewer reports are available.

Reprints and permission information is available at <http://www.nature.com/reprints>

Publisher's note Springer Nature remains neutral with regard to jurisdictional claims in published maps and institutional affiliations.



Open Access This article is licensed under a Creative Commons Attribution 4.0 International License, which permits use, sharing, adaptation, distribution and reproduction in any medium or format, as long as you give appropriate credit to the original author(s) and the source, provide a link to the Creative Commons license, and indicate if changes were made. The images or other third party material in this article are included in the article's Creative Commons license, unless indicated otherwise in a credit line to the material. If material is not included in the article's Creative Commons license and your intended use is not permitted by statutory regulation or exceeds the permitted use, you will need to obtain permission directly from the copyright holder. To view a copy of this license, visit <http://creativecommons.org/licenses/by/4.0/>.

© The Author(s) 2021